

Under review, "IEEE Trans. Geoscience and Remote Sensing"

# A New Shape-Based Method for Object Localization and Characterization from Scattered Field Data \*

Eric L. Miller, Misha Kilmer, and Carey Rappaport  
Dept. of Electrical and Computer Engineering  
Northeastern University  
360 Huntington Ave.  
Boston, MA 02215  
Tel: (617) 373-8386  
email: elmiller@cdsp.neu.edu

July 22, 1999

## Abstract

The problem of characterizing the structure of an object buried in an inhomogeneous half-space of unknown composition is considered. We develop a non-linear inverse scattering algorithm based on a low dimensional parameterization of the unknown object and the background. In particular, we use low order polynomials to represent the contrast in the real and imaginary parts of the object and background complex permittivities. The boundary separating the target from the unknown background is described using a periodic, quadratic B-spline curve whose control points can be individually manipulated. We determine the unknown control point locations and contrast expansion coefficients using a greedy-type approach to minimize a regularized least-squares cost function. The regularizer used here is designed to constrain the geometric structure of the boundary of the object and is closely related to snake methods employed in the image processing community. We demonstrate the performance of our approach via extensive numerical simulation involving 2D,  $TM_z$  scattering geometries.

---

\*This work was supported by an OSD MURI on Demining under Grant DAAG55-97-1-0013 and a CAREER Award from the National Science Foundation, MIP-9623721

# 1 Introduction

We consider the problem of localizing and characterizing the structure of an object buried in a halfspace given noisy observations of scattered electromagnetic fields collected near the interface. Such problems arise in application areas including environmental remediation, humanitarian demining, medical imaging and non-destructive testing [6, 11, 14, 26]. Here we are particularly concerned with addressing two of the many challenges associated with such inverse scattering problems. First, these problems are known to be highly ill-posed in that the quantity of information contained in the data, which are collected only near the interface, is quite limited relative to the amount of information one would like to extract. This leads to considerable instabilities in terms of reliably characterizing the behavior of the subsurface [21, 25]. A second difficulty is the need to deal with *clutter*. Here we take clutter to be physical characteristics of the medium, in particular volume inhomogeneities, whose presence impedes our ability to characterize the object of interest.

Typical methods for overcoming these two problems are based on forming an image of the subsurface and then post processing the results to extract target information [5, 27]. The issue of ill-posedness is addressed through the use of a regularization procedure [3, 23, 25] to stabilize the imaging portion of the algorithm while clutter suppression is achieved through the use of image processing methods to separate targets from background. In forming an image, however, one must solve a large scale, non-linear optimization problem whose size is equal to the number of pixels (voxels) in the region of interest; a highly computationally intensive process. Moreover, under this approach one uses the limited data to generate values for all of the pixels only a few of which contain useful information about the underlying target. By diffusing the information in the data in this manner, target detection can be problematic [24].

There has been considerable work in the past decade on methods that extract directly from the data geometric information regarding the shape and location of the object [8–13, 19, 21, 22, 29, 32].

The assumption underlying most of these methods is that the object is embedded in a medium of otherwise known structure (homogeneous or halfspace). Rather than parameterizing the problem in terms of a large number of pixel values, a relatively small number of unknowns are used to describe the shape of the target. For these methods the issue of ill-posedness is either addressed through a regularization procedure related to the shape of the object [21] or through the use of more traditional Tikhonov or minimum norm least squares methods [11, 15, 32].

For our problems, these shape-based methods are not applicable. For example, the approach taken in [13] requires that the object be surrounded on all sides by transmitters and receivers. While this assumption is satisfied in, for example, medical imaging applications, we are restricted here to problems where we have only reflection-type data at our disposal. Additionally, most of the previously developed techniques assume that the electrical properties of the background are fully known and in many cases, the object's contrast function is also specified *a priori* [22]. Because we wish to address the issue of volume inhomogeneity, we must look to a different approach.

Hence we consider a parameterization based on a concise description of the object's geometric structure that provides for the recovery of a limited amount of information regarding the spatial variations of the complex permittivity over the target and the background. As described in § 2, the variations in the background and the object contrast are modeled via a superposition of a small number of expansion functions; one set of functions for the background and separate set for the object. Thus, the unknowns here are the corresponding expansion coefficients.

As in [1, 11, 21], we seek a representation for the shape of the object in terms of a small number of unknowns. In previous work, a Fourier-type expansion is used in conjunction with an underlying assumption that the object of interest is star-like. Here we choose to describe the boundary of the objects differently, using a linear combination of quadratic B-splines [4, Chap. 3]. The motivation for this choice comes from the fact that the parameters governing this representation (known as

control points) impact the shape of the object only over a small portion of the perimeter. Thus, the control points provide direct and local control over the object's shape. This control is exploited in the development of a simple and efficient inversion scheme described in § 3. Finally, the control-point parameterization leads to a natural, shape-based regularization technique related to *snake* methods [4] used in image processing for contour representation and image segmentation.

We view this approach as a compromise between an ill-posed imaging method that allows for arbitrary variation throughout the region and the more constrained shape-based methods in which homogeneity is assumed. By restricting the contrast variations to lie within the linear span of a set of basis functions, we clearly limit the classes of variations which can be recovered from this inversion process. The motivation for this decision comes from the fact that a detailed reconstruction of the medium is often not what is desired nor is it supported by the information in the data. Rather, the primary information of interest concerns the geometric structure of the object. Thus we are willing to settle for a coarse reconstruction of the object and background contrast functions.

The remainder of this paper is arranged as follows. In § 2, the scattering problem and the models for the object and background are presented; § 3 gives a presentation of the inversion procedure with examples of its performance shown in § 4. Conclusions and future work are described in § 5.

## 2 Problem formulation

We consider a two-dimensional scattering problem illustrated in Fig. 1. Time harmonic  $e^{-j\omega t}$   $y$ -polarized plane waves at various incident angles and frequencies are used to probe the medium. The complex permittivity of the lower halfspace is represented as the sum of a nominal, constant value,  $\epsilon_1 + (j/\omega)\sigma_1$ , and a space varying perturbation,

$$g(\mathbf{r}) = \epsilon_0 \epsilon_p(\mathbf{r}) + \frac{j}{\omega} \sigma_p(\mathbf{r}), \quad (j = \sqrt{-1}), \quad (1)$$

that encompasses both the object of interest as well as the clutter. Here,  $\mathbf{r} = [x \ z]^T$  is a two vector indicating the position of a point in the plane,  $\epsilon_0$  is a constant that denotes the permittivity of free space, and  $\omega$  denotes angular frequency. The scattered fields generated by  $g$  are observed along an array of point receivers also located in the upper halfspace. Under this 2D model, there is only a single component of the electric field thereby resulting in a scalar scattering problem.

The model linking the structure of  $g$  to the observed scattered field at the  $k$ th point along the array,  $\mathbf{r}_k$ , is [7, Chap. 9]

$$y(\mathbf{r}_k) = \omega^2 \mu_0 \int_W G(\mathbf{r}_k, \mathbf{r}') E(\mathbf{r}') g(\mathbf{r}') d\mathbf{r}' + n(\mathbf{r}_k), \quad (2)$$

where  $y(\mathbf{r}_k)$  is the datum at  $\mathbf{r}_k$  for a given incident field,  $W$  is the region over which  $g$  is nonzero,  $n$  is zero mean, additive white Gaussian measurement noise with variance  $\zeta^2$ , and  $G$  and  $E$  denote the Green's function and total electric field, respectively. The constant  $\mu_0$  denotes the permeability of free space. In (2), we are only concerned with evaluating the Green's function,  $G(\mathbf{r}, \mathbf{r}')$ , when  $\mathbf{r}$  is above the interface and  $\mathbf{r}'$  is below in which case [10]

$$G(\mathbf{r}, \mathbf{r}') = \frac{j}{2\pi} \int_{-\infty}^{\infty} \frac{1}{\gamma_0 + \gamma_1} \exp [j\alpha(x - x') + j(\gamma_1 z - \gamma_0 z')] d\alpha \quad (3)$$

with  $\gamma_i = (k_i^2 - \alpha)^{1/2}$  where  $k_i = \omega \sqrt{\epsilon_i \mu_0 + j\sigma_i \mu_0 / \omega}$  denotes the wavenumber in the upper ( $i = 0$ ) and lower ( $i = 1$ ) halfspace. The total electric field  $E(\mathbf{r})$  is governed by the Helmholtz equation

$$[\nabla^2 + k^2(\mathbf{r})] E = 0$$

with a Sommerfeld radiation condition where  $k^2(\mathbf{r})$  is equal to  $k_0^2$  above the interface and  $k_1^2 + \omega^2 \mu_0 g(\mathbf{r})$  below. Finally, the total electric field at  $\mathbf{r}$  is the sum of the unperturbed electric field generated by a plane wave impinging on a halfspace,  $E_{unp}(\mathbf{r})$ , [20, § 3.2] and the scattered electric field,  $E_s(\mathbf{r})$ . With  $E = E_s + E_{unp}$ , it is easy to show that:

$$[\nabla^2 + k^2(\mathbf{r})] E_s = -\omega^2 \mu_0 g(\mathbf{r}) E_{unp}. \quad (4)$$

As  $y(\mathbf{r})$ , the observed field, depends on the total field in the region  $W$ , it therefore implicitly depends on the particular unperturbed field,  $E_{unp}$ , on  $g(\mathbf{r})$ , and on the frequency  $\omega$ .

## 2.1 A Model for $g(\mathbf{r})$

As described in the introduction, we model the unknown portion of the permittivity in the lower halfspace as a superposition of a slowly varying, compactly supported anomaly (the target) on a background of partially known structure (clutter). Mathematically  $\epsilon_p(\mathbf{r})$  is decomposed as

$$\epsilon_p(\mathbf{r}) = S(\mathbf{r}) \sum_{i=1}^{N_a} a_{1,i} b_{1,i}(\mathbf{r}) + [1 - S(\mathbf{r})] \sum_{i=1}^{N_b} a_{2,i} b_{2,i}(\mathbf{r}) \equiv S(\mathbf{r}) B_1(\mathbf{r}) \mathbf{a}_1 + [1 - S(\mathbf{r})] B_2(\mathbf{r}) \mathbf{a}_2 \quad (5)$$

where  $S(\mathbf{r})$  is one over the (unknown) support of the object and zero elsewhere. The functions  $b_{1,i}$  represent basis functions describing the contrast of the real part of the anomaly while the  $b_{2,i}$  do the same but for the background. The  $a_{i,j}$  are the expansion coefficients determining the weight of each function. The row vectors  $B_i$ ,  $i = 1, 2$  hold the expansion functions and  $\mathbf{a}_i$  are vectors of expansion coefficients. An analogous model holds for  $\sigma_p(\mathbf{r})$ , which is proportional to the imaginary portion of  $g(\mathbf{r})$ :

$$\sigma_p(\mathbf{r}) \equiv S(\mathbf{r}) B_1(\mathbf{r}) \mathbf{c}_1 + [1 - S(\mathbf{r})] B_2(\mathbf{r}) \mathbf{c}_2. \quad (6)$$

While in principle the expansion functions could differ between  $\epsilon_p$  and  $\sigma_p$ , the support function  $S$  is the same since it represents a physical boundary between the object and the rest of the medium.

The particular choice of the  $b_{i,j}$  depends on the application at hand. If one thought that there was a homogeneous dielectric anomaly of contrast  $a_{1,1}$  against a real-valued homogeneous background of value  $a_{2,1}$  then one would take  $b_{1,1}(\mathbf{r}) = b_{2,1}(\mathbf{r}) = 1$ . Use of higher order polynomials, trigonometric functions etc. provide greater flexibility in capturing true, underlying inhomogeneities. In any event, assuming the  $B_i$  are known, the objective of the problem in this paper is to determine the structure of  $S$  along with the  $\mathbf{a}_i$  and  $\mathbf{c}_i$  given the observed scattered field data.

In this work, we employ a B-spline model to describe the contour of the anomaly, that is, the boundary of the set  $S(\mathbf{r})$ . To define this curve, we start with an interval  $[0, L]$  on which a *knot* sequence  $k_0, \dots, k_{K-1}$  with  $0 \leq k_i \leq L$  is defined. For this sequence, there exists a periodic basis

of quadratic B-splines  $C_{k_i}(s)$  such that

$$b(s) \equiv [x(s), z(s)] = \sum_{i=0}^{K-1} C_{k_i}(s)[x_i, z_i], \quad s \in [0, L] \quad (7)$$

for a given set of  $x_i, z_i$  expansion coefficients, or *control points*, uniquely defines a closed,  $C^2$  parametric curve in the plane. The support of each  $C_{k_i}(s)$  is  $[k_i, k_{i+3}]$ . Since the basis is taken to be periodic, the control points are assumed to be wrapped; that is,  $[x_0, z_0] = [x_{K-2}, z_{K-2}]$  and  $[x_1, z_1] = [x_{K-1}, z_{K-1}]$ , so there are a total of  $K$  control points,  $K - 2$  of which are unique.

To implement our model, we assume that the boundary of the anomaly is in the form:

$$b^*(s) \equiv \sum_{i=0}^{K-1} C_{k_i}(s)[x_i^*, z_i^*]. \quad (8)$$

If  $\mathbf{r} = [x \ z]^T$  is a point inside  $b^*(s)$ , then for example,  $\epsilon_p(\mathbf{r})$  is  $B_1(\mathbf{r})\mathbf{a}_1$ , while for  $\mathbf{r}$  outside,  $\epsilon_p(\mathbf{r}) = B_2(\mathbf{r})\mathbf{a}_2$ .

### 3 Algorithm

In this section we describe in detail the algorithm we use to solve the inverse problem. We begin by discussing the discretized form of the model. The reader is referred to Table 1 for a summary of the indexing parameters that have been or will be identified.

#### 3.1 Discretization

Using the method of moments [17] with a pulse basis and point matching to discretize (2) and a lexicographical ordering of the unknowns yields the matrix equation:

$$\mathbf{y} = \mathbf{G}\mathcal{D}(\mathbf{E})\mathbf{g} + \mathbf{n}, \quad \mathbf{y} \in C^{M \times 1} \quad (9)$$

where  $M$  is the number of source/receiver pairs,  $\mathbf{y}$  and  $\mathbf{n}$  are vectors with components  $y(\mathbf{r}_k)$  and  $n(\mathbf{r}_k)$  respectively,  $\mathbf{G}$  the discrete Green's function premultiplied by  $\omega^2\mu_0$ ,  $\mathcal{D}(\cdot)$  is the diagonal matrix formed from the vector argument, and  $\mathbf{E}$  is the vector containing the total electric field (which depends on  $\mathbf{g}$ ) at each pixel. Finally,  $\mathbf{g} \in C^{N \times 1}$  is a vector holding the intensity values of

$g(\mathbf{r})$  at the  $N$  grid points in our discretization of the subsurface and from (5) and (6) is given as:

$$\mathbf{g} = \epsilon_0[\mathbf{S}\mathbf{B}_1 - (\mathbf{I} - \mathbf{S})\mathbf{B}_2]\mathbf{a} + \frac{j}{\omega}[\mathbf{S}\mathbf{B}_1 - (\mathbf{I} - \mathbf{S})\mathbf{B}_2]\mathbf{c} \equiv \left[ \epsilon_0\mathbf{V} \quad \frac{j}{\omega}\mathbf{V} \right] \mathbf{w} \quad (10)$$

where  $\mathbf{a} = [\mathbf{a}_1^T \quad \mathbf{a}_2^T]^T$ ,  $\mathbf{c} = [\mathbf{c}_1^T \quad \mathbf{c}_2^T]^T$ ,  $\mathbf{w} = [\mathbf{a}^T \quad \mathbf{c}^T]^T$ ,  $\mathbf{S}$  is a diagonal matrix corresponding to  $S$  with  $\mathbf{S}_{i,i} = 1$  if any part of pixel  $i$  is inside  $b^*(r)$  and 0 otherwise,  $\mathbf{I}$  is the identity matrix, and the  $\mathbf{B}_i$  denote the  $N \times N_a$  and  $N \times N_b$  matrices corresponding to evaluating  $B_i(r)$  at the  $N$  gridpoints.

Finally, using  $\mathbf{A} = \mathbf{G}\mathcal{D}(\mathbf{E})$  with (10) and (9) we have

$$\mathbf{y} = [\epsilon_0\mathbf{A}\mathbf{V}, \quad \frac{j}{\omega}\mathbf{A}\mathbf{V}]\mathbf{w} + \mathbf{n} \equiv \mathbf{K}\mathbf{w} + \mathbf{n}, \quad \mathbf{y} \in C^{M \times 1}. \quad (11)$$

Note that there is one such matrix-vector equation of this form for each frequency and each different incident angle. In the remainder of the paper, we assume  $n_1$  frequencies and  $n_2$  angles are used, and we use double superscripts  $i, k$  to denote the corresponding vectors and matrices at frequency  $\omega_i$  and angle  $\theta_k$ : single superscripts imply that that quantity depends only on  $\omega_i$ . For example,  $\mathbf{y}^{i,k}$  denotes the data obtained via (9) or (11) for frequency  $\omega_i$  and incident angle  $\theta_k$

$$\mathbf{y}^{i,k} = \mathbf{G}^i \mathcal{D}(\mathbf{E}^{i,k}) \mathbf{g}^i + \mathbf{n}^{i,k} = \mathbf{K}^{i,k} \mathbf{w} + \mathbf{n}^{i,k}, \quad (12)$$

whereas  $\mathbf{g}^i$  denotes (10) at frequency  $\omega_i$ .

### 3.2 Generating Scattered Field

To generate the data for a given frequency  $\omega_i$  and incident angle  $\theta_j$ , we need to compute the  $M$ -length vector  $\mathbf{E}^{i,j}$  (i.e. we need to solve the forward scattering problem). To do this, we determine the scattered field by discretizing (4) using a finite difference scheme with PML boundary condition (details are described in [18]) to obtain the matrix equation  $\mathbf{M}^i \mathbf{E}_s^{i,j} = -\omega_i^2 \mu_0 \mathbf{g}^i \mathbf{E}_{unp}^{i,j}$  where the unperturbed field  $\mathbf{E}_{unp}^{i,k}$  is known and depends on incident angle and frequency, and  $\mathbf{M}^i$  is the matrix corresponding to the discretized operator in (4) with the PML boundary condition. The scattered field is determined by solving the matrix equation for  $\mathbf{E}_s^{i,j}$ , and finally,  $\mathbf{E}^{i,j} = \mathbf{E}_{unp}^{i,j} + \mathbf{E}_s^{i,j}$ .



### 3.3 Algorithm Description

Our algorithm seeks to find a good approximation to  $g(\mathbf{r})$  by successively generating better and better approximations to  $b^*(s)$ , the boundary of the anomaly, and the coefficient vectors  $\mathbf{a}$  and  $\mathbf{c}$ .

In particular, we seek a minimum of the following cost function

$$J(b(s), \mathbf{a}, \mathbf{c}) = \sum_{i=1}^{n_1} \sum_{k=1}^{n_2} \|\mathbf{y}^{i,k} - \mathbf{G}^i \mathcal{D}(\mathbf{E}^{i,k}) \mathbf{g}^i\|_2^2 + \lambda_1 \Omega_1(b(s)) + \lambda_2 \Omega_2(b(s)). \quad (13)$$

where we emphasize that both  $\mathbf{E}^{i,j}$  as well as  $\mathbf{g}^i$  depend implicitly on the geometry of the anomaly as well as the expansion vectors via the models developed in § 2 and § 3.1. The first term in (13) enforces fidelity to the data while the second and third play the role of regularizers.

Traditional regularization methods used to combat ill-posedness in an image restoration framework function by enforcing smoothness, or in some cases edge preservation, in the reconstruction. In our case, the  $\Omega_i, i = 1, 2$  are used to influence the geometric structure of the recovered anomaly. Specifically, we define these functions as

$$\Omega_1(b(s)) = \sum_{i=0}^{K-2} (z_i - z^*)^2 \quad \text{and} \quad \Omega_2(b(s)) = \sum_{i=0}^{K-2} (x_i - x_{i+1})^2 + (z_i - z_{i+1})^2 \quad (14)$$

where  $K$  is the total number of control points,  $x_i$  and  $z_i$  are the coordinates of the  $i$ th control point, and  $z^*$  is a fixed  $z$ -value depending on the particular application. The first term attempts to penalize objects that are too deep while the second penalizes the total length between control points. In this way we dissuade the algorithm from choosing curves that are overly elongated and/or deep. Our justification for the first of these choices comes from our knowledge that significant depth information is not available in the measured data due to the loss in the soil and the positioning of detectors only above the interface. Moreover, in most applications one possesses some *a priori* information concerning the depth at which targets are likely to be buried. The values of  $\lambda_1, \lambda_2$  tell how strongly we want to dissuade the algorithm from reconstruction of curves that are too elongated and/or deep. Finding near optimal regularization parameters is a very difficult problem and there is a whole body of literature dedicated to this issue (see, for instance, [2, 16]). In this work, we assume

that good parameters are known *a priori*: determining accurate parameter selection strategies will be the subject of future work.

We consider a greedy-type algorithm for minimizing (13). We begin with an initial estimate,  $b^{(0)}(s)$ , of  $b^*(s)$  defined by a set of  $K$  knots and  $K - 2$  distinct control points. From  $b^{(0)}(s)$  the matrix  $\mathbf{S}$  is found. Suppose for the moment that initial estimates of  $\mathbf{a}, \mathbf{c}$ , denoted  $\mathbf{a}^{(0)}, \mathbf{c}^{(0)}$ , are known (we address the issue of generating these guesses below). Using (10), the  $\mathbf{g}^i$  are calculated for the different frequencies. We then use (13) to determine the cost of  $(b^{(0)}, \mathbf{a}^{(0)}, \mathbf{c}^{(0)})$ .

We update the estimate of  $b^{(0)}(s)$  by systematically perturbing each control point from its original position by a fixed amount  $\bar{h}$  in the horizontal, vertical, and diagonal directions, respectively, for a total of 8 different moves per point. Note that each of these 8 moves corresponds to a new curve by definition in (7). Since there are  $K - 2$  unique points and 8 moves for each point, this corresponds to  $8(K - 2)$  different possible new curves. For each possible curve, we first estimate new values for  $\mathbf{a}$  and  $\mathbf{c}$  and then evaluate the cost associated with the current curve and these estimates using (13). Finally,  $b^{(1)}(s)$ ,  $\mathbf{a}^{(1)}$ , and  $\mathbf{c}^{(1)}$ , our new estimates, are taken as that triple giving minimum cost, provided that cost is less than (or equal to) the cost associated with  $(b^{(0)}(s), \mathbf{a}^{(0)}, \mathbf{c}^{(0)})$ . The process is repeated as many times as is necessary.

In principle, determination of  $\mathbf{a}$  and  $\mathbf{c}$  requires the solution of a low dimensional inverse scattering problem. That is, every time we want to determine the cost for a candidate curve, we need to solve a non-linear optimization problem. To simplify this procedure, we consider an alternative approach. At the end of the  $k$ th stage, we compute the internal fields associated with the current estimate of the anomaly. This requires the solution of  $n_1 n_2$  forward scattering problems of size  $N$ . From (9), the data  $\mathbf{y}^{i,l}$  depend on the anomaly through  $\mathbf{g}^i$  and the internal fields. At stage  $k + 1$ , we assume that as we move the control points to generate new candidate structures, the changes in the internal fields are negligible compared to the changes in the  $\mathbf{g}^i$ . Thus, for each of these candidates,

we hold the internal fields fixed at the values computed at the end of the previous stage.

This approach is useful for two reasons. First, it reduces the number of forward solves associated with each iteration from  $8(K-2)n_1n_2$  to just  $n_1n_2$ . Second, by holding the internal fields fixed, (9) and (11) indicate that the unknown expansion coefficients are locally *linearly* related to the data. Thus, estimates of these quantities can be obtained via a linear least squares procedure that is far less demanding than a nonlinear optimization problem. In particular, we have

$$\hat{\mathbf{w}} = \arg \min_{\mathbf{w}} \|\mathbf{K}\mathbf{w} - \mathbf{y}\|_2^2 = (\mathbf{K}^T\mathbf{K})^{-1}\mathbf{K}^T\mathbf{y} \quad (15)$$

where  $\mathbf{K}$  is the matrix obtained by stacking all of the real and imaginary parts of  $\mathbf{K}^{i,k}$  defined in (11) and (12) and (with a slight abuse of notation)  $\mathbf{y}$  is the corresponding stacked real and imaginary parts of  $\mathbf{y}^{i,k}$ .

Now we address the choice of  $\mathbf{a}^{(0)}, \mathbf{c}^{(0)}$ . Solving (15) requires  $\mathbf{K}$ , which by (11) requires  $\mathbf{A}^{i,k}$ , which in turn requires  $\mathbf{E}^{i,k}$ . But computing  $\mathbf{E}^{i,k}$  according to §3.2 would require prior knowledge of the unknown  $\mathbf{g}^i$ . Thus, to get initial estimates of the expansion coefficients, we set  $\mathbf{E}^{i,k}$  to  $\mathbf{E}_{unp}^{i,k}$ ; in other words, we use the Born approximation to determine initial guesses of  $\mathbf{a}^{(0)}, \mathbf{c}^{(0)}$ .

The algorithm is initialized using an object of size larger than any target of interest located in the vicinity of the true object. There are many possible methods for determining such an initial guess. For example, there are methods that determine a “best fit” disk as an initialization: one based on array processing is described in [28] while another based on statistical hypothesis testing is detailed in [24]. Here, we always assume that the initial object is given and refer the reader to the literature for specific techniques to determine this guess.

The overall algorithm is sketched in Fig. 2. One advantage of this approach is that it is quite easy to implement and in principle, all candidates at any given stage can be generated in parallel. Thus it is computationally attractive. It is not difficult to prove that if we were to recompute the internal fields for each possible control point move (rather than leaving it fixed at the previous

estimate), then we would be guaranteed that at every outer iteration of our algorithm the cost would be non-increasing. By insuring old curves cannot be regenerated<sup>1</sup>, this would imply convergence of the algorithm to a minimum of (13) taken over the collection of anomalies that can be generated by these moves. However, since we hold the internal fields fixed as we loop over control point moves and update them only after a move is chosen, monotonicity of the cost cannot be guaranteed. Generally, we have noticed through extensive simulation that as long as the parameters  $\lambda_1$  and  $\lambda_2$  are well chosen, the cost does in fact decrease as the iterations progress.

## 4 Numerical Examples

In this section we present several numerical examples that illustrate the effectiveness of our algorithm. All experiments were done in Matlab using double precision arithmetic. Creation and manipulation of the B-spline curves was achieved with Matlab's Spline Toolbox.

In all of the numerical examples, we used three frequencies (500, 700, and 900 MHz) and three incident angles ( $0, \pi/4, -\pi/4$ ). The region of interest for which we would like to obtain an image was 40cm across (-20cm to 20cm) and 20 cm deep (0 to 20cm). We discretized this region into pixels of size 1cm-by-1cm. Data were collected at 19 receivers located at -18cm to 18cm in 2cm increments. To define the entries of the Green's function matrix  $G$ , we set  $\epsilon_1 = 2.5\epsilon_0, \sigma_1 = 3E - 3$ , which corresponds to assuming that the upper halfspace is air and the lower halfspace is sand. Depending on the example, we fill the  $B_i(\mathbf{r})$  matrices of (5) and (6) with monomials of at most degree 2. Finally, Table 2 summarizes the parameters for each of the experiments. The values for the  $\lambda_i$  were chosen by trial and error. In all experiments, the value of the step size,  $\bar{h}$ , was taken to be one centimeter. Finally, the contours of all the true objects were generated using a B-spline with  $K = 6$  knots while the reconstructions were generated for a  $K = 5$  knot contour.

---

<sup>1</sup>It turns out that our approach to updating the internal electric field can create the situation in which distinct curves yield the same cost. Thus we implement extra logic in our implementation to ensure that we never enter a loop.

To produce noisy data, independent additive Gaussian noise was added to both the real and imaginary parts of the noise free data. Letting  $\tilde{\mathbf{y}}$  denote the vector obtained by stacking  $\mathbf{K}^{i,j}\mathbf{w}$  for all frequencies and incident angles we have  $\mathbf{y} = \tilde{\mathbf{y}} + \mathbf{n}$  where  $\mathbf{n} = \zeta_r \mathbf{n}_r + j\zeta_i \mathbf{n}_i$  and  $\mathbf{n}_r, \mathbf{n}_i$  were generated using Matlab's `randn` function. The constants  $\zeta_r, \zeta_i$  were determined so that the signal-to-noise ratio (SNR) with respect to the real and imaginary parts of  $\tilde{\mathbf{y}}$  were the same:

$$SNR = 10 \log_{10} \frac{\text{real}(\tilde{\mathbf{y}})^T \text{real}(\tilde{\mathbf{y}})}{\zeta_r N} = 10 \log_{10} \frac{\text{imag}(\tilde{\mathbf{y}})^T \text{imag}(\tilde{\mathbf{y}})}{\zeta_i N}.$$

We used two measures of success in comparing our reconstructions with the true images. The first is a relative error measure over all pixels in the union of the true curve and the reconstructed curve, which we index by the index set  $\mathcal{I}$ :

$$SE = \frac{\|\epsilon_{true}(\mathcal{I}) - \epsilon_p(\mathcal{I})\|^2}{\|\epsilon_{true}(\mathcal{I})\|^2} + \frac{\|\sigma_{true}(\mathcal{I}) - \sigma_p(\mathcal{I})\|^2}{\|\sigma_{true}(\mathcal{I})\|^2}$$

For each example, we also recorded the maximum pointwise relative error in the real (imaginary) part of the solution over the pixels in the intersection of the true and reconstructed curves. The values for these measures for the 5 examples described below are in Table 4.

#### 4.1 Examples 1 and 2: Homogeneous Perturbations

As a first example, we consider the problem with a homogeneous object of unknown contrast embedded in a homogeneous half-space at an SNR of 20 dB, Fig. 3(a)–(b). While the inversion scheme knows the correct basis function to use for the object and background (i.e.  $N_a = 1 = N_b$  in (5) and (6) with  $b_{1,1} = 1 = b_{2,2}$  in both cases) it still does not know the values of the expansion coefficients. In Fig. 3(e) we display the true boundary of the object along with the initial guess of this quantity and the final boundary estimate produced by our algorithm. The true and estimated images of the  $\epsilon_p$  and  $\sigma_p$  for this problem are shown in Fig. 3(c)–(d) where we observe that the unknown contrasts are estimated quite accurately. This conclusion is supported by the numerical values for our figures of merit given in Table 4.

For comparison sake, we have also implemented a more traditional Born iterative method (BIM)

[31] inversion procedure using a TSVD (truncated singular value decomposition) regularization technique to stabilize the linear system that must be solved at each iteration. After optimizing the regularization parameter for this procedure, the reconstructions of the real and imaginary parts of  $\mathbf{g}$  are shown in Figs. 4.

This example demonstrates that even under noisy circumstances, the approach we have proposed is able to capture accurately both the shape and the numerical values of the unknown permittivity and conductivity of the object. While the BIM clearly indicates the presence of an object in  $\epsilon_p$ , almost nothing is seen in the  $\sigma_p$  image. Further, note that the anomaly boundary is much less well reconstructed compared to our new approach. Also, numerous artifacts appear in both parts of the reconstruction. By constraining the reconstruction as is done in our algorithm, we obtain a much more accurate representation of the true profile. Our reconstructed object differs from the true by only four pixels. Moreover, the amplitudes of  $\epsilon_p$  and  $\sigma_p$  are quite close to their true values.

The performance of our approach is further verified in Fig. 5 where we display boundary curves and true and estimated images of  $\epsilon_p$  and  $\sigma_p$  for an object rotated relative to the interface. The BIM plots are shown in Fig. 6. The same level of performance as was seen in the previous example is also seen here. Moreover, because we reconstruct the boundary explicitly, this approach allows us to easily characterize the orientation of the buried object, a potentially useful piece of information for later processing stages concerned with identification and classification.

## 4.2 Cramer-Rao Bounds for Examples 1 and 2

We next turn our attention to more challenging problems in which the electrical properties of both the background and the object can vary. A first issue of concern is construction of the  $B$  matrices used to model these variations. Intuitively, we expect that that as the size of the object falls, it will be increasingly difficult to recover higher order information about the target structure when the profile of the much larger background region is also unknown. In fact, we can quantify

the validity of this idea using the notion of a Cramer-Rao bound (CRB).

As explained more fully in [30, § 2.4], the CRB provides a lower bound on the variance of any unbiased parameter estimator in a noisy data information extraction procedure of the type considered here. The CRB is a deterministic quantity reflecting the nature of the physical model, the parameterization of the problem, and statistics of the noise corrupting the data. While we make no claims here concerning the bias of our estimator, the CRB provides a useful gauge as to the maximum confidence we should have in the numerical values of the  $\mathbf{a}$  and  $\mathbf{c}$  estimates produced by our algorithm. Specifically, by examining the bounds for different configurations of object and background, we obtain insight into how we may want to structure our inversion algorithm.

Here we consider our ability to recover information concerning at most linear variations in both the background and the object, i.e. cases in which the real or imaginary parts of these quantities behave as  $d_0 + d_1 x + d_2 z$  where the  $d_j$  can represent any of the  $a_{i,j}$  or  $c_{i,j}$  coefficients appearing in the model of § 2.1. This level of complexity is sufficient to understand the basic issues. In particular, we consider CRB information for objects of three sizes with linear contrast variations (shown in Fig. 7) embedded in backgrounds whose variations are also linear. Fig. 8 illustrates the configurations of interest for the medium size object. The SNR for all experiments is 30 dB.

The numerical values of the square roots of the CRBs (i.e. the lower bounds on the standard deviations) for the experiments are provided in Table 3. The first column refers to the coefficient in the model. For example, the row beginning “Object real: const.” holds the information regarding the true value and the bound on the constant coefficient in the real part of the object. Similarly, “Bkgnd real: x” is the row for the coefficient governing the real part of the  $x$  variation in the background. In all cases, the bounds on the coefficients governing the background are a small fraction of the true values and vary little with the size of the embedded object. These small bounds imply small variance in the estimates of the background structure and thus indicate that we can

in fact determine these quantities rather accurately. This is true both for the constant term in the variation as well as the linear terms. In contrast, our ability to recover anything but the unknown constant term describing the object is more limited. The bounds on the  $x$  and  $z$  coefficients are at best on the order of the true values and grow at a much more rapid rate as the object size decreases making determination of these quantities a very delicate procedure.

With this in mind, in the remainder of this paper (with the exception of Example 5) we consider object models comprised of only unknown constants. As we show below, even when the true object is of a more complex structure, the use of this simple model still allows for accurate localization and the recovery of limited quantitative information. In light of the underlying objective of our approach, we view this tradeoff of accuracy in “pixel” space for accuracy in localization and geometric characterization as acceptable. In terms of specifying the model for the background, the situation is less clear. Extensive numerical experiments (not reported here) indicate that one needs a relatively accurate model to achieve good localization. That is, the order of the model should approximate well the true distribution of the volume inhomogeneity. As a rigorous solution to the model order determination problem is outside of the scope of this paper, here we consider only models whose order meets or exceeds that of the true distribution.

### 4.3 Examples 3-5

The next example we consider is illustrated in Fig. 9. Here we have an object with a piecewise constant profile in a background with linear variation. We invert using a model for a constant object and a quadratic background variation. The values for the object are intended to represent a dielectric scatterer with an air gap. It is important to note that this object can never be well represented using our low order polynomial model. The results of inverting with a model employing a constant object with a quadratic background are shown in Figs. 10(c)–(e). The strong localization performance demonstrated in these images in spite of this inherent model mismatch points to the



robustness of our approach to inversion <sup>2</sup>.

A similar experiment was repeated except that the values for the real and imaginary parts of the background were each corrupted by small amounts of appropriately scaled  $[0, 1]$  additive uniform noise. Now neither the object nor the background can be exactly represented using the polynomial model. As shown in Fig. 10 we achieve highly accurate shape information along with useful information concerning the variations in the object as well as the background. Again, these results are indicative of the ability of a low order parameterization to withstand modeling inaccuracies. We note that for both of these examples, the results in Table 4 reflect the fact that we have sacrificed contrast accuracy for geometric fidelity. However, by modeling the contrasts as unknown constant, as expected we obtain estimated values that are close to the average values of the actual perturbations (which can be positive or negative) over the support of the anomaly. In Example 3 the computed real and imaginary perturbations are  $8.9\text{E-}2$  and  $-2.5\text{E-}2$ , respectively, compared to the means of the true perturbations to the real and imaginary parts,  $8.3\text{E-}2$  and  $-2.3\text{E-}3$ . Likewise, for Example 4 the calculated real and imaginary parts over the anomaly are  $5.8\text{E-}3$  and  $-7.01\text{E-}3$  whereas the means of the true real and imaginary parts are  $2\text{E-}2$  and  $-2.4\text{E-}3$ .

Finally, in Fig. 11 we consider the problem of recovering a linearly varying object in a linearly varying background. Motivated by the CRB results, the object here is taken to be larger than those of the previous examples so that there will be sufficient signal to allow us to resolve the permittivity variations. As in the other cases, we again achieve strong localization. However there is some noticeable error in the estimates of the permittivity coefficients which is a reflection of the inherent difficulty in accurately obtaining this information. This example points to the need for further work in refining the permittivity estimates after having determined the boundary of the

---

<sup>2</sup>For this and the remaining experiments, we do not show the results of the BIM approach to inversion. Even after extensive fine tuning of the algorithm, it was impossible to obtain results comparable to those seen with the currently considered method.

object: model order determination and low order parameterizations should both play a role.

## 5 Conclusions and Future Work

We presented a new and potentially efficient technique for simultaneously solving the image formation and object characterization problems from scattered electric field data. The key idea was to formulate the perturbation in terms of a small number of parameters via a B-spline representation for the contour of the target. The examples illustrated that our technique can lead to good quality reconstructions: in particular, we found that it was possible to get good localization information even if the background is not homogeneous. A key issue associated with this strong performance is the ability to select good regularization parameters that balance the information content of the data with that of the constraints. In this work, we selected those parameters by hand. Clearly, an important area of future effort is the automation of this process.

Our experiments showed and the computed Cramer-Rao bounds confirmed that it is difficult, if not impossible, to get “linear” or even more complex information about the object unless it was sufficiently large, the noise sufficiently small, and the perturbation in the object was large relative to the perturbation in the background (i.e. the background needs to be nearly homogeneous).

One potential computational advantage to our technique is its inherent parallelism: cost evaluations can be done in parallel, making it computationally feasible to consider more complicated structures. For our reconstruction technique to capture more complex structures, however, we need to consider how to alter the complexity of the boundary representation by inserting and deleting basis elements in the B-spline representation. Solving this order determination problem in an efficient and close to optimal manner is far from trivial. In the future, we will also consider extensions of this work to the case of multiple objects. Finally, we hope to extend the work presented here to the 3D problem and to analyze its performance on real data.

## References

- [1] T. S. Angell, Xinming Jiang, and R. E. Kleinman. A distributed source method for inverse acoustic scattering. *Inverse Problems*, (13):531–545, 1997.
- [2] Murat Belge, Eric Miller, and Misha Kilmer. Simultaneous multiple regularization parameter selection by means of the l-hypersurface with applications to linear inverse problems posed in the wavelet transform domain. In *SPIE International Symposium on Optical Science, Engineering, and Instrumentation: Bayesian Inference for Inverse Problems*. SPIE, July 1998.
- [3] M. Bertero, C. De Mol, and E. R. Pike. Linear inverse problems with discrete data, II, Stability and regularisation. *Inverse Probl.*, 4:573–594, 1988.
- [4] Andrew Blake and Michael Isard. *Active Contours*. Springer, 1998.
- [5] W. C. Chew, G. P. Otto, W. H. Weedon, J. H. Lin, C. C. Lu, Y. M. Wang, and M. Moghaddam. Nonlinear diffraction tomography: The use of inverse scattering for imaging. *International Journal of Imaging Systems and Technology*, 7:16–24, 1996.
- [6] W.C. Chew and Y. M. Wang. Reconstruction of two-dimensional permittivity distribution using the distorted born iterative method. *IEEE Trans. Medical Imaging*, 9(2):218–225, June 1990.
- [7] Weng Cho Chew. *Waves and Fields in Inhomogeneous Media*. Van Nostrand Reinhold, New York, 1990.
- [8] Weng Cho Chew and G. Otto. Microwave imaging of multiple conducting cylinders using local shape function. *IEEE Microwave Guided Wave Letters*, 2:284–284, 1992.
- [9] Chien-Ching Chiu and Yean-Woei Kiang. Electromagnetic imaging for and imperfectly conducting cylinder. *IEEE Trans. Microwave Theory and Techniques*, 39(9):1632–1639, September 1991.
- [10] Chien-Ching Chiu and Yean-Woei Kiang. Inverse scattering of a buried conducting cylinder. *Inverse Problems*, 7:187–202, 1991.
- [11] Chien-Ching Chiu and Yean-Woei Kiang. Electromagnetic inverse scattering of a conducting cylinder buried in a lossy half-space. *IEEE Trans. on Antennas and Propagation*, 40(12), Augusts 1992.
- [12] Chien-Ching Chiu and Yean-Woei Kiang. Microwave imaging of multiple conducting cylinders. *IEEE Trans. on Antennas and Propagation*, 40(8), August 1992.
- [13] David Colton and Andreas Kirsch. A simple method for solving inverse scattering problems in the resonance region. *Inverse Problems*, 12:383–393, 1996.
- [14] David Colton and Peter Monk. The detection and monitoring of leukemia using electromagnetic waves: mathematical theory. *Inverse Problems*, 10:1235–1251, 1994.
- [15] David Colton, Michele Piana, and Roland Potthast. A simple method using Morozov’s discrepancy principle for solving inverse scattering problems. *Inverse Problems*, (13):1477–1493, 1997.

- [16] Per Christian Hansen. Analysis of discrete ill-posed problems by means of the L-curve. *SIAM Review*, 34(4):561–580, December 1992.
- [17] R. F. Harrington. *Field Computations by Moment Methods*. Macmillan, New York, 1968.
- [18] Misha Kilmer, Eric Miller, and Carey Rappaport. Preconditioners for structured matrices arising in subsurface object detection. *Journal of Computational Physics*. in review.
- [19] Andreas Kirsch. Characterization of the shape of a scattering obstacle using the spectral data of the far field operator. *Inverse Problems*, 14:1489–1512, 1998.
- [20] Jin Au Kong. *Electromagnetic Wave Theory*. John Wiley and Sons, 1986.
- [21] G. Kristensson and C. R. Vogel. Inverse problems for acoustic waves using the penalized likelihood method. *Inverse Problems*, 2:461–479, 1986.
- [22] A. Litman, D. Lesselier, and F. Santosa. Reconstruction of a two-dimensional binary obstacle by controlled evolution of a level-set. *Inverse Problems*, 14:685–706, 1998.
- [23] Pierre Lobel, Laure Blanc-Feraud, Christian Pichot, and Michel Barlaud. New regularization scheme for inverse scattering. *Inverse Problems*, 13(2):403–410, April 1997.
- [24] Eric L. Miller. Statistically based methods for anomaly characterization in images from observations of scattered radiation. *IEEE Trans. on Image Processing*, 8(1):92–101, January 1999.
- [25] Eric L. Miller, Lena Nicolaides, and Andreas Mandelis. Nonlinear inverse scattering methods for thermal wave slice tomography: A wavelet domain approach. *Journal of the Optical Society of America (A)*, 1998.
- [26] Lena Nicolaides and Andreas Mandelis. Image-enhanced thermal-wave slice diffraction tomography with numerically simulated reconstructions. *Inverse Problems*, 13(5):1339–1412, 1997.
- [27] Christian Pichot, Pierre Lobel, Cedric Dourthe, Laure Blanc-Feraud, and Michel Barlaud. Microwave inverse scattering: Quantitative reconstruction of complex permittivity for different applications. *IEICE Transactions on Electronics*, E80-C:1343–1348, November 1997.
- [28] Adnan Sahin and Eric L. Miller. Electromagnetic scattering-based array processing methods for near-field object characterization. *Journal of Electromagnetic Waves and Applications*, 13:1209–1236, 1999.
- [29] L. Souriau, B. Duchene, D. Lesselier, and R. E. Kleinman. Modified gradient approach to inverse scattering for binary objects in stratified media. *Inverse Problems*, (12):463–481, 1996.
- [30] Harry L. Van Trees. *Detection, Estimation and Modulation Theory: Part I*. John Wiley, New York, 1968.
- [31] Y. M. Wang and W. C. Chew. An iterative solution to the two-dimensional electromagnetic inverse scattering problem. *International Journal of Imaging Systems and Technology*, 1(1):100–108, 1989.
- [32] William H. Weedon and Weng Cho Chew. Time-domain inverse scattering using the local shape function (LSF) method. *Inverse Problems*, 9:551–564, 1993.

$K$	total number of control points ( $K - 2$ unique)
$n_1$	number of frequencies used to probe the earth
$n_2$	number of angles used to probe the earth
$N$	number of unknowns in subsurface discretization
$M$	number of data points for given $\theta, \omega$
$NM$	total number of data points
$N_a$	number columns in $\mathbf{B}_1$
$N_b$	number columns in $\mathbf{B}_2$

Table 1: Summary of index parameters. Note that the degrees of polynomials used to represent the object and the background are  $N_a - 1$  and  $N_b - 1$ , respectively.

Example	SNR	True Obj.	True Back	Obj.	Back	$\lambda_1$	$\lambda_2$
1	20dB	0	0	0	0	3.28E-4	1.59E-4
2	20dB	0	0	0	0	6.0E-5	6.0E-5
3	30dB	PWC	1	0	2	1.55E-4	7.9E-5
4	20dB	PWC	1,rand	0	2	9.0E-5	6.0E-5
5	30dB	1	0	1	0	4.0762E-4	1.7015E-4

Table 2: Summary of experiments. Numbers in columns 3 to 6 indicate the degree of the polynomial used to generate the data (columns 3,4) or to reconstruct (columns 5,6). “PWC” indicates that the true object had piecewise constant perturbations in both the real and imaginary parts. “rand” indicates that random uniform perturbations were added to the real and imaginary parts of the background when generating data.

Coefficient		(True)	(Large)	(Medium)	(Small)
		Value	Bound	Bound	Bound
Object	real: const	4E-1	7.43E-2	3.42E-1	4.27
	real: x	1	1.02	2.56	4.57E+1
	real: z	8	9.17E-1	5.18	9.29E+1
	imag: const	-2.2E-3	3.09E-3	3.11E-2	8.57E-1
	imag: x	1E-2	4.22E-2	1.08E-1	2.05
	imag: z	4E-2	4.98E-2	7.09E-1	2.06E+1
Bkgnd	real: const	-1E-1	2.42E-2	2.14E-2	1.71E-2
	real: x	1	1.72E-1	1.58E-1	1.51E-1
	real: z	4	2.09E-1	2.00E-1	1.89E-1
	imag: const	-1E-3	8.93E-4	7.99E-4	7.32E-4
	imag: x	0	6.95E-3	6.15E-3	5.80E-3
	imag: z	1E-2	8.25E-3	7.45E-3	7.35E-3

Table 3: Values of the bounds for the case when the background and the object BOTH vary linearly (at 30dB). Note that the bounds for all 3 linear terms for the object dramatically increase as the size of the object decreases, whereas the bounds for the background decrease only slightly.

Ex.	SE	RE (real)	RE (imag)
1	0.335	0.110	0.607
2	0.593	0.367	0.616
3	1.051	1.059	0.172
4	6.182	1.191	2.565
5	1.447	3.185	0.085

Table 4: Measures of success in reconstruction. First column gives the experiment number and second column gives the error measure defined in the beginning of § 4. Last two columns give maximum pointwise relative error for the real and imaginary parts, respectively, over the pixels in the intersection between the true and reconstructed images.

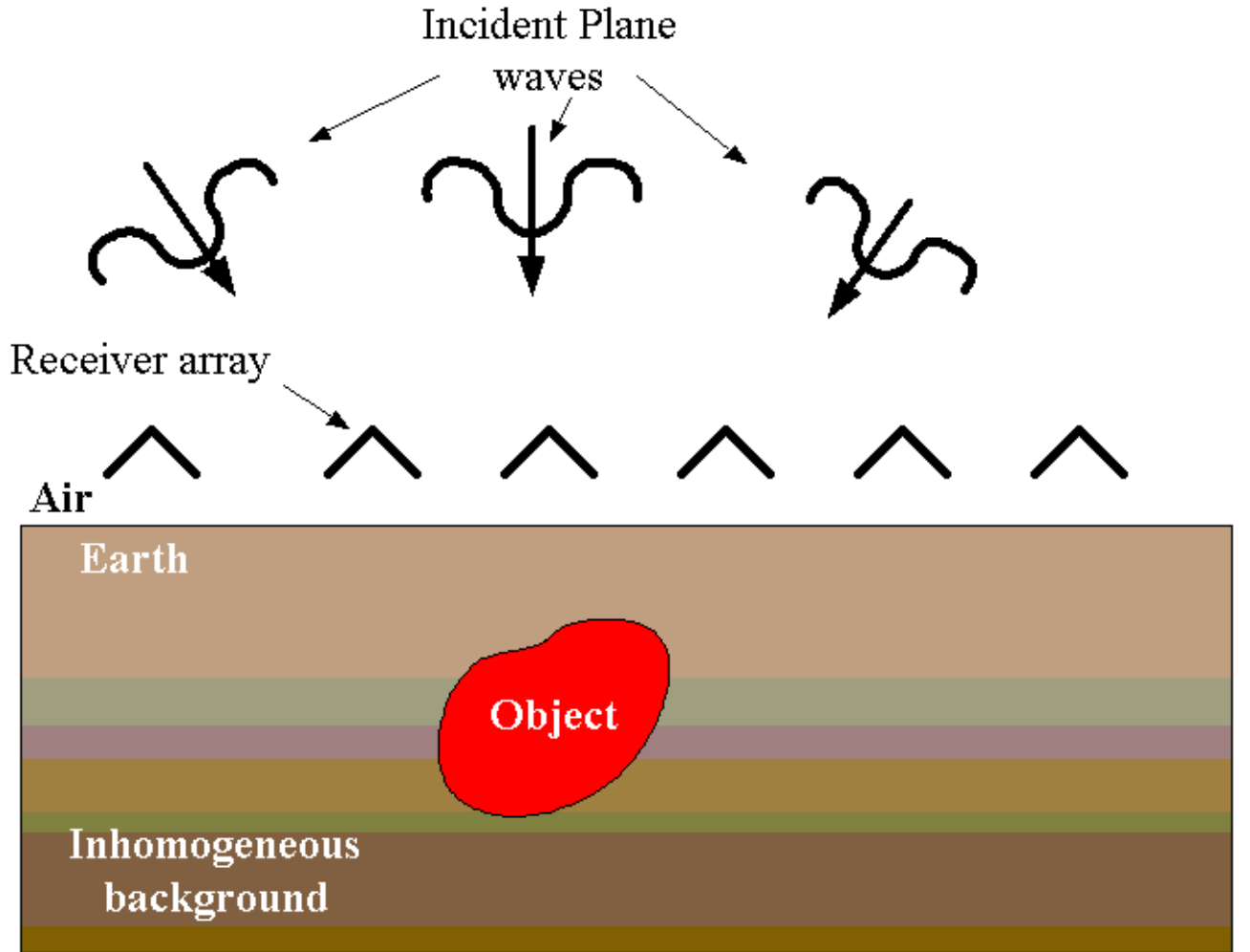


Figure 1: Experimental configuration for general problem of interest

**Algorithm 1**

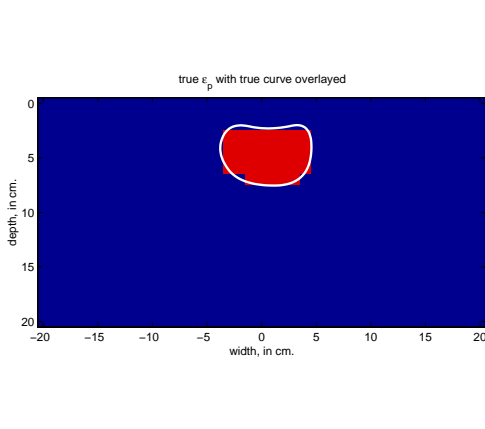
```

 $k := 1$ 
Given initial estimates  $[b^{(1)}(s), \mathbf{a}^{(1)}, \mathbf{c}^{(1)}]$  compute  $\mathbf{E}^{i,j}$  and  $\mathbf{A}^{i,j}$  for  $1 \leq i \leq n_1, 1 \leq j \leq n_2$ 

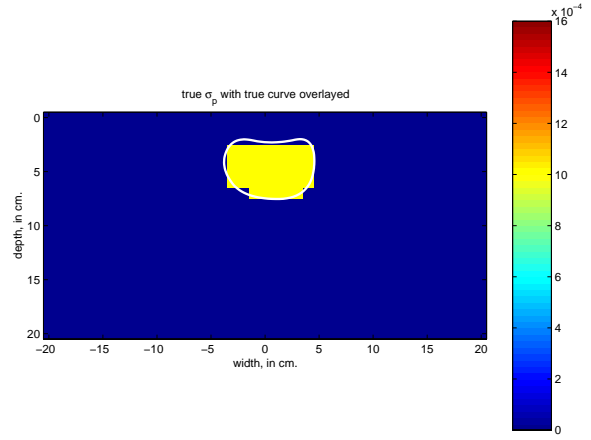
While (current-cost can still be reduced) do
    • For  $i = 0, \dots, K - 3$  do
        1. Select control point  $(x_i, z_i)$ 
        2. For each of 8 moves of  $(x_i, z_i)$  by  $\bar{h}$  do
            (a) Update  $(x_i, z_i)$  by a move
            (b) Form candidate contour,  $b(s)$ , from other control points and new version
                of  $(x_i, z_i)$ 
            (c) Generate estimates  $\hat{\mathbf{a}}, \hat{\mathbf{c}}$  using current  $\mathbf{A}^{i,j}$  (see (15))
            (d)  $\text{cost} := J(b(s), \hat{\mathbf{a}}, \hat{\mathbf{c}})$  (see (9) and (13))
            (e) If  $\text{cost} < \text{current-cost}$ 
                 $b^{(k)}(s) := b(s); \text{current-cost} := \text{cost}; [\mathbf{a}^{(k)}, \mathbf{c}^{(k)}] := [\hat{\mathbf{a}}, \hat{\mathbf{c}}]$ 
            (f) Elseif  $\text{cost} = \text{current-cost}$ 
                If  $b(s)$  is different from all previous  $b^{(k)}(s)$ ,
                 $b^{(k)}(s) := b(s); [\mathbf{a}^{(k)}, \mathbf{c}^{(k)}] := [\hat{\mathbf{a}}, \hat{\mathbf{c}}]$ 
        • From  $[b^{(k)}(s), \mathbf{a}^{(k)}, \mathbf{c}^{(k)}]$  compute  $\mathbf{E}^{i,j}$  and  $\mathbf{A}^{i,j}$  for  $1 \leq i \leq n_1, 1 \leq j \leq n_2$ 
        • Update  $[\mathbf{a}^{(k)}, \mathbf{c}^{(k)}]$  using the new  $\mathbf{A}^{i,j}$ 
        •  $\text{current-cost} := J(b^{(k)}(s), \mathbf{a}^{(k)}, \mathbf{c}^{(k)})$ 
        •  $k := k + 1$ 
end while

```

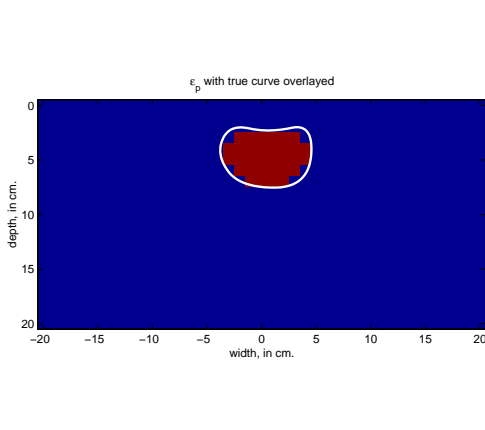
Figure 2: Anomaly Recovery Algorithm



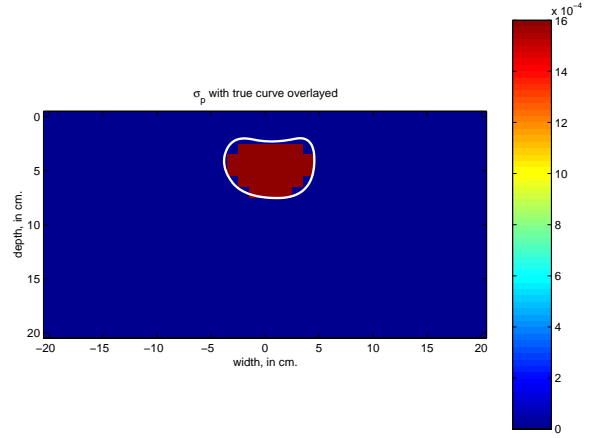
(a) True distribution for  $\epsilon_p(\mathbf{r})$



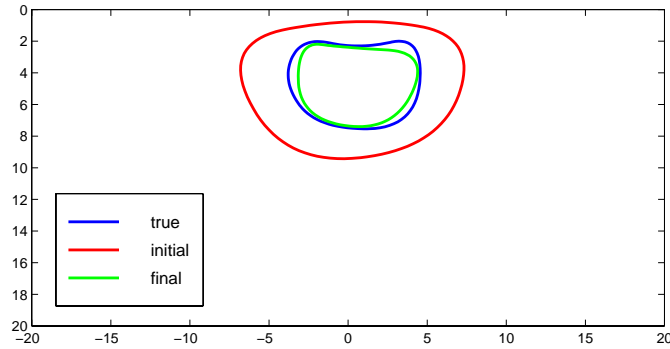
(b) True distribution for  $\sigma_p(\mathbf{r})$



(c) Estimate of  $\epsilon_p(\mathbf{r})$



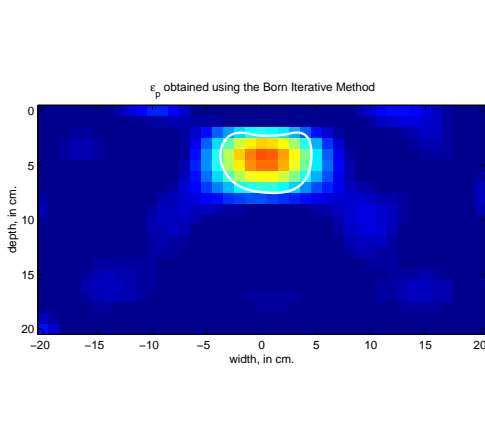
(d) Estimate of  $\sigma_p(\mathbf{r})$



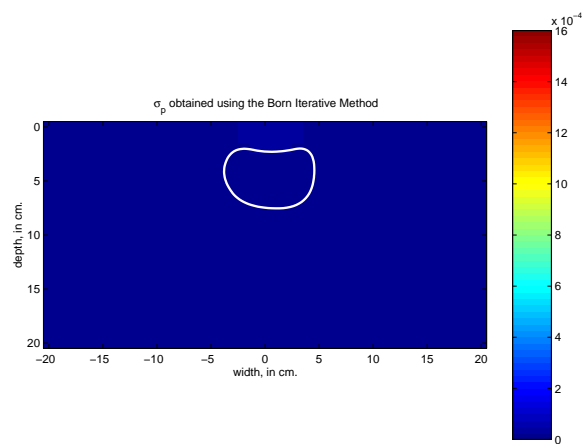
(e) Initial guess, final estimate, and true object boundary

Figure 3: True distributions, estimates, and boundary structures for example 1 (parameters given in Table 2).



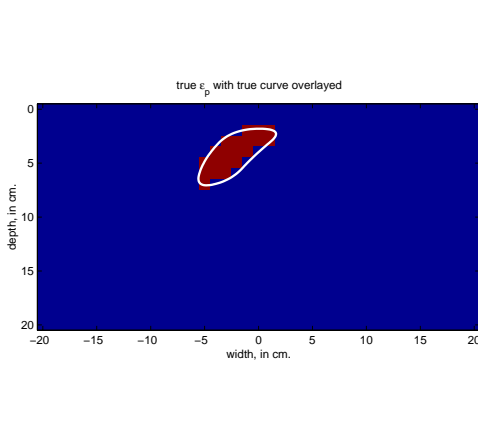


(a) Estimate of  $\epsilon_p(\mathbf{r})$

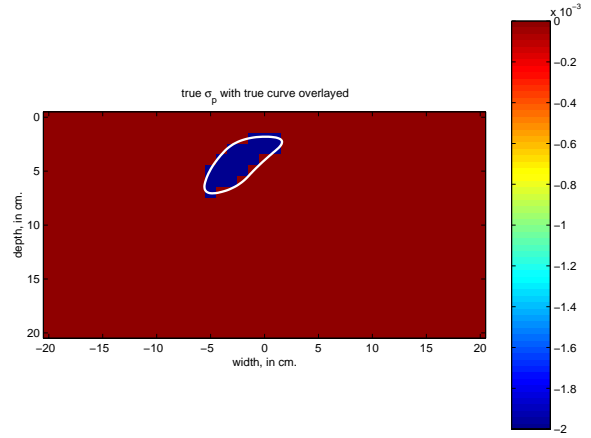


(b) Estimate of  $\sigma_p(\mathbf{r})$

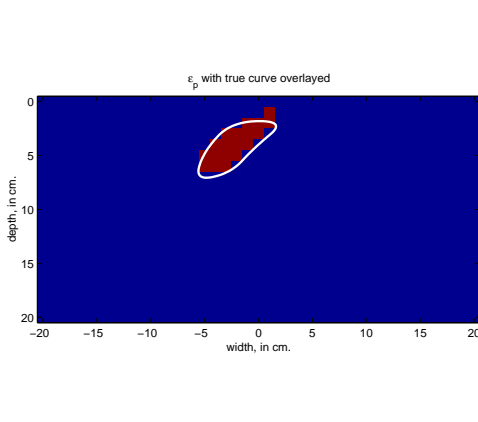
Figure 4: Born iterative results for example 1



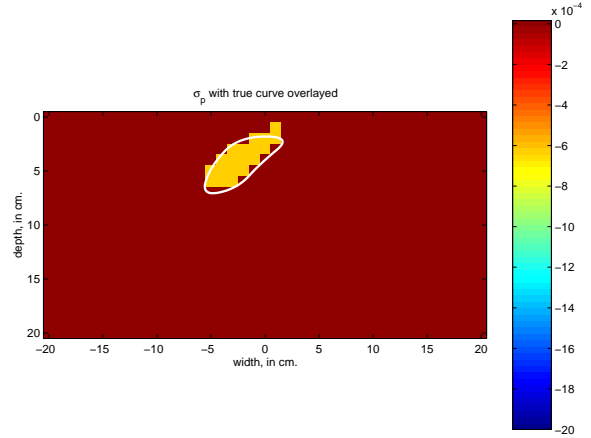
(a) True distribution for  $\epsilon_p(\mathbf{r})$



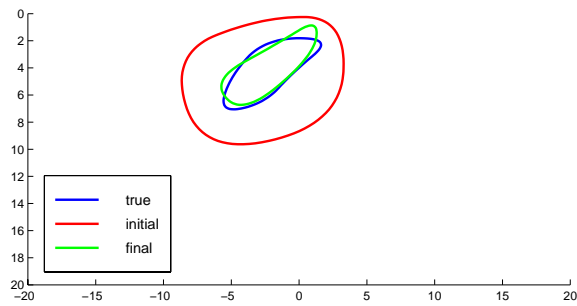
(b) True distribution for  $\sigma_p(\mathbf{r})$



(c) Estimate of  $\epsilon_p(\mathbf{r})$



(d) Estimate of  $\sigma_p(\mathbf{r})$



(e) Initial guess, final estimate, and true object boundary

Figure 5: True distributions, estimates, and boundary structures for example 2 (parameters given in Table 2).

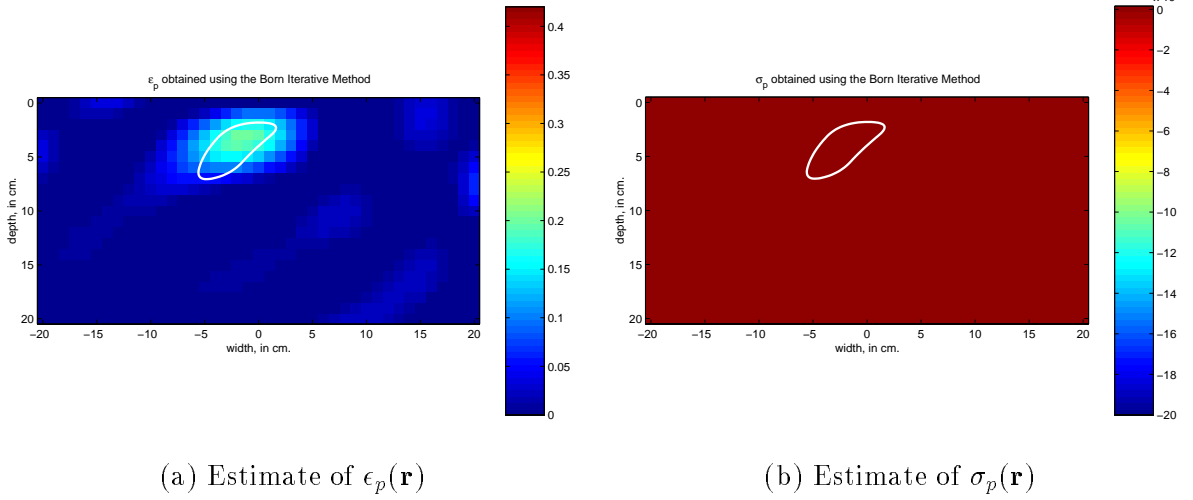


Figure 6: Born iterative results for example 2.

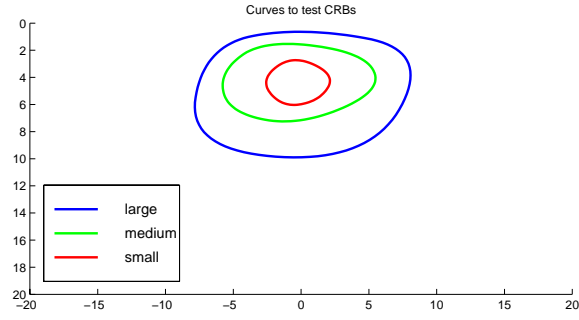


Figure 7: Three boundary curves used to evaluate Cramer Rao bound information

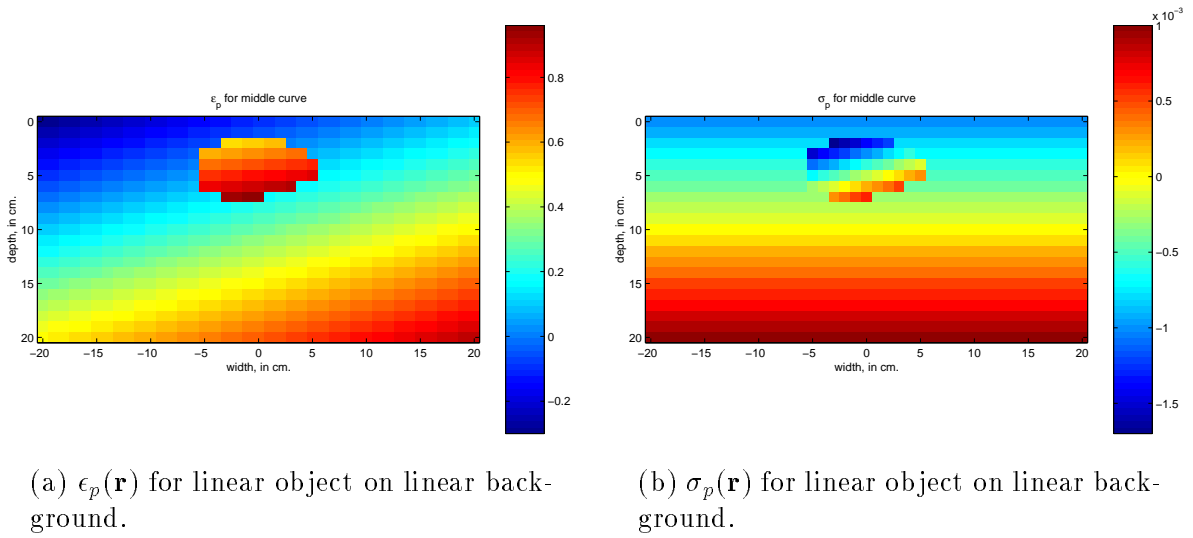
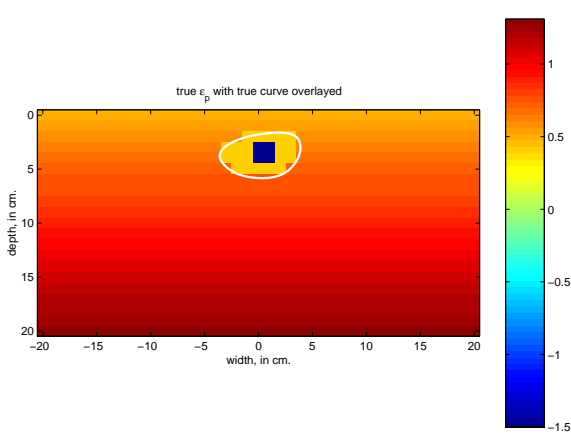
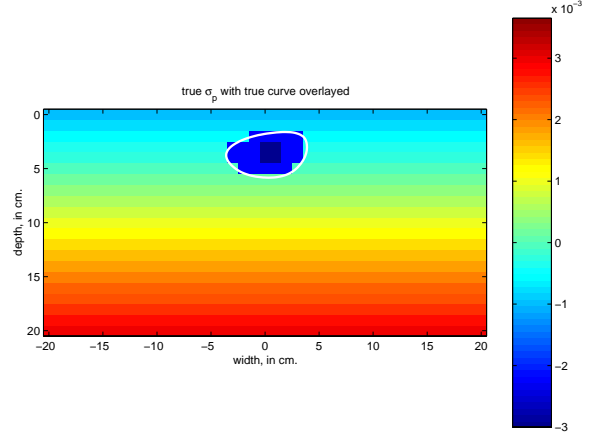


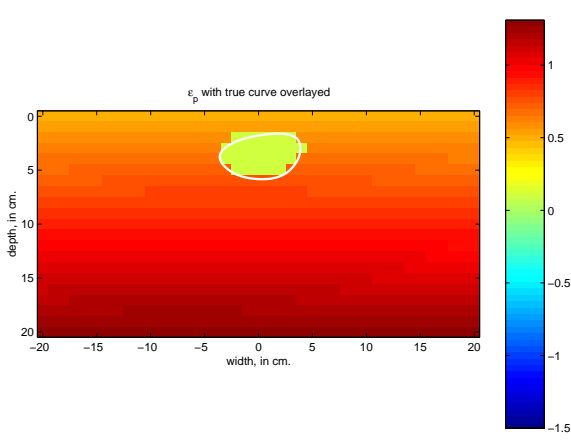
Figure 8: Permittivity distributions for medium size object CRB analysis.



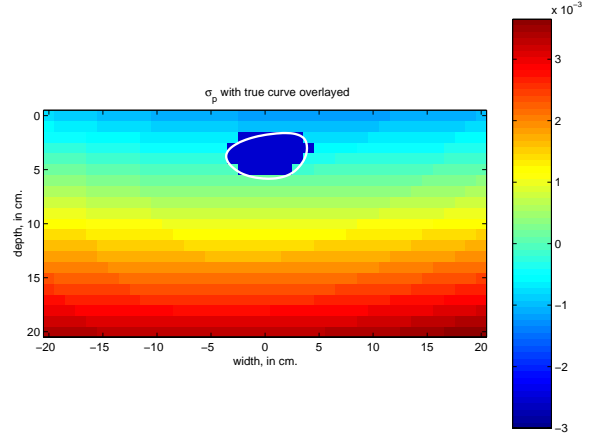
(a) True distribution for  $\epsilon_p(\mathbf{r})$



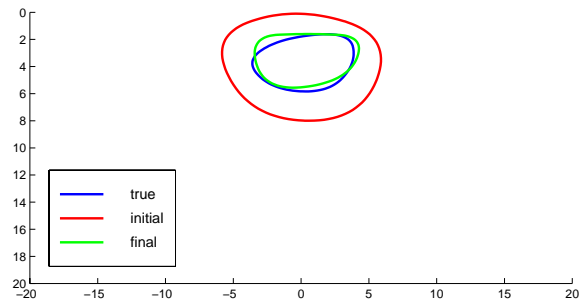
(b) True distribution for  $\sigma_p(\mathbf{r})$



(c) Estimate of  $\epsilon_p(\mathbf{r})$

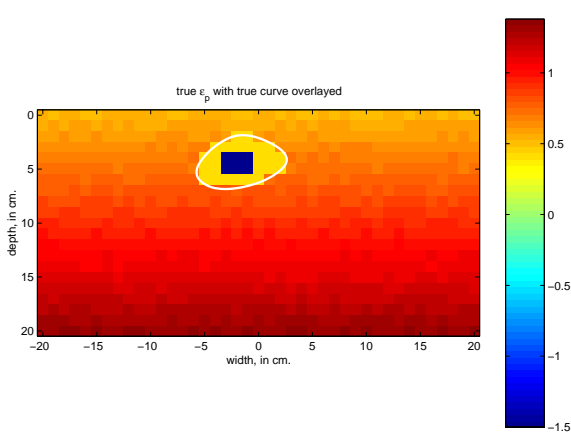


(d) Estimate of  $\sigma_p(\mathbf{r})$

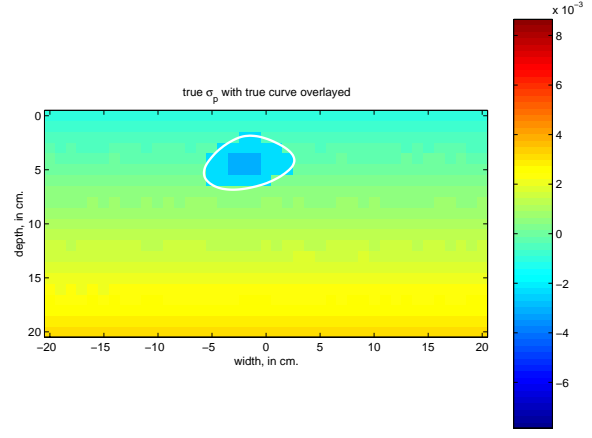


(e) Initial guess, final estimate, and true object boundary

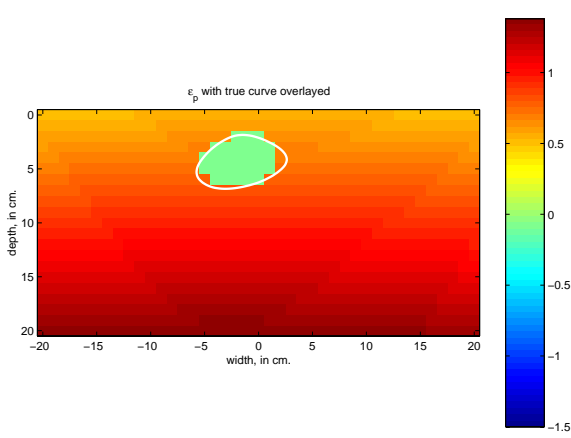
Figure 9: True distributions, estimates, and boundary structures for example 3 (parameters given in Table 2).



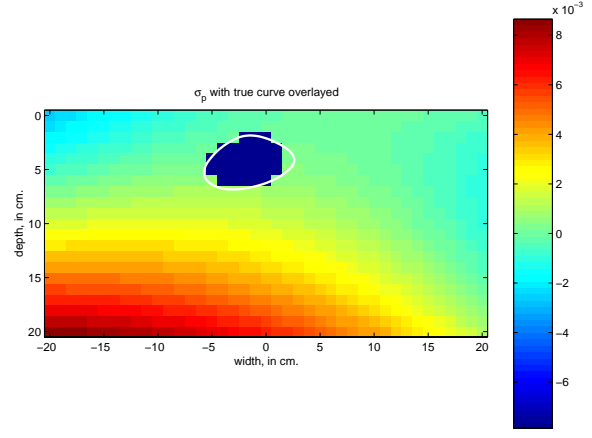
(a) True distribution for  $\epsilon_p(\mathbf{r})$



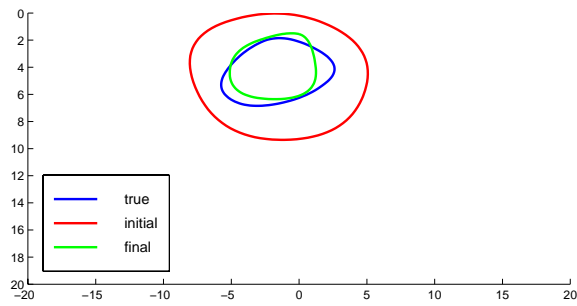
(b) True distribution for  $\sigma_p(\mathbf{r})$



(c) Estimate of  $\epsilon_p(\mathbf{r})$

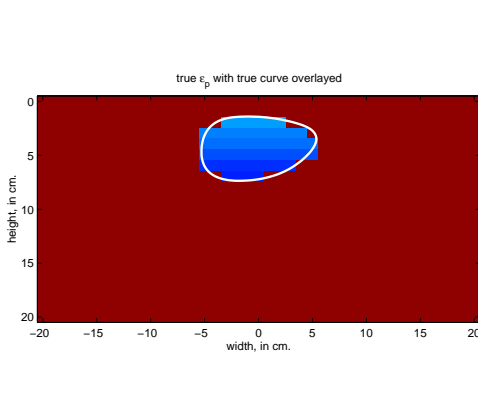


(d) Estimate of  $\sigma_p(\mathbf{r})$

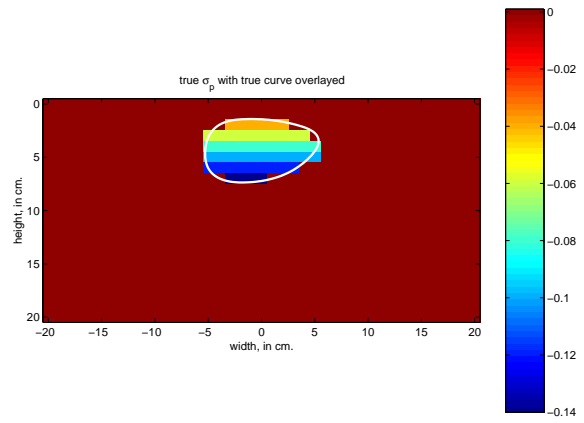


(e) Initial guess, final estimate, and true object boundary

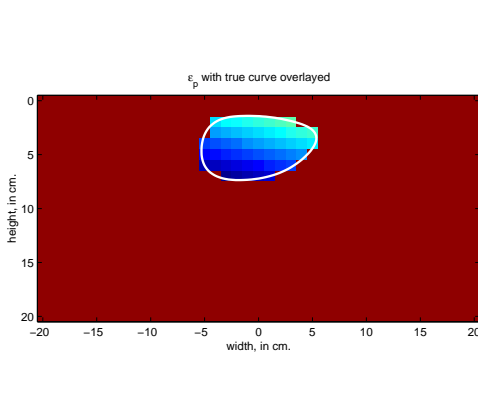
Figure 10: True distributions, estimates, and boundary structures for example 4 (parameters given in Table 2).



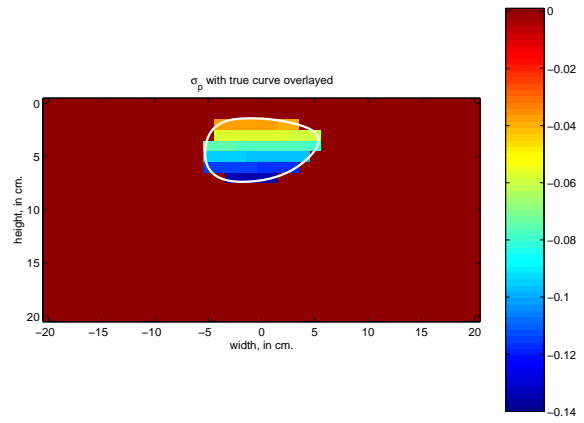
(a) True distribution for  $\epsilon_p(\mathbf{r})$



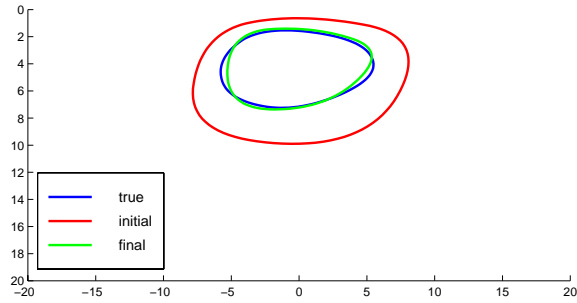
(b) True distribution for  $\sigma_p(\mathbf{r})$



(c) Estimate of  $\epsilon_p(\mathbf{r})$



(d) Estimate of  $\sigma_p(\mathbf{r})$



(e) Initial guess, final estimate, and true object boundary

Figure 11: True distributions, estimates, and boundary structures for example 5 (parameters given in Table 2).